



**HAL**  
open science

## Cross-calibration and first vertical ECE measurement of electron energy distribution in the TCV tokamak

A Tema Biwole, L Porte, A Fasoli, L Figini, J Decker, M Hoppe, J  
Cazabonne, L Votta, A Simonetto, S Coda

► **To cite this version:**

A Tema Biwole, L Porte, A Fasoli, L Figini, J Decker, et al.. Cross-calibration and first vertical ECE measurement of electron energy distribution in the TCV tokamak. *Plasma Physics and Controlled Fusion*, 2024, 66 (12), pp.125010. 10.1088/1361-6587/ad88a0 . cea-04816316

**HAL Id: cea-04816316**

**<https://cea.hal.science/cea-04816316v1>**

Submitted on 3 Dec 2024








**HAL** is a multi-disciplinary open access archive for the deposit and dissemination of scientific research documents, whether they are published or not. The documents may come from teaching and research institutions in France or abroad, or from public or private research centers.

L'archive ouverte pluridisciplinaire **HAL**, est destinée au dépôt et à la diffusion de documents scientifiques de niveau recherche, publiés ou non, émanant des établissements d'enseignement et de recherche français ou étrangers, des laboratoires publics ou privés.



Distributed under a Creative Commons Attribution 4.0 International License

# Cross-calibration and first vertical ECE measurement of electron energy distribution in the TCV tokamak

A Tema Biwole<sup>1,5,\*</sup> , L Porte<sup>1</sup>, A Fasoli<sup>1</sup> , L Figini<sup>2</sup> , J Decker<sup>1</sup> , M Hoppe<sup>3</sup> , J Cazabonne<sup>4</sup> , L Votta<sup>3</sup>, A Simonetto<sup>2</sup>, S Coda<sup>1</sup>  and the TCV Team<sup>6</sup>

<sup>1</sup> Ecole Polytechnique Fédérale de Lausanne (EPFL), Swiss Plasma Center (SPC), CH-1015 Lausanne, Switzerland

<sup>2</sup> Istituto per la Scienza e Tecnologia dei plasmi, Via Roberto Cozzi 53, Milano (MI), 20125, Italy

<sup>3</sup> KTH Royal Institute of Technology, Department of Electrical Engineering, Stockholm, Sweden

<sup>4</sup> Commissariat à l'énergie Atomique, CEA-IRFM, F-13108 Saint-Paul-les-Durance, France

E-mail: [biwole@mit.edu](mailto:biwole@mit.edu)

Received 25 July 2024, revised 18 September 2024

Accepted for publication 18 October 2024

Published 4 November 2024



## Abstract

This paper describes the first vertical electron cyclotron emission measurement of non-thermal electron distributions in the *Tokamak à Configuration Variable*. These measurements were conducted in runaway electron scenarios and in the presence of electron cyclotron current drive. Measured intensities of linearly polarized X- and O-mode radiation from fast electrons allow the analysis of the energy distribution. The measurements were made possible through the creation of an operational regime for the diagnostic that is free of thermal background radiation, in relaxed electron density operations. This operational regime notably enables the cross-calibration of the diagnostic system, relying on thermal plasma measurements and modeling with the ray-tracing code SPECE.

Keywords: electron cyclotron emission, non-thermal electron distribution, runaway electron, electron cyclotron current drive, radiometry, calibration, synthetic diagnostics

## 1. Introduction

Electron Cyclotron Emission (ECE) is a well-established technique for measuring electron temperature in tokamaks [1, 2]. The conditions for such measurement generally include a

thermal plasma, i.e. a plasma in which the electron distribution can be assumed Maxwellian, and optically thick conditions for the electron cyclotron wave. For temperature measurement, when these conditions are fulfilled, ECE configurations are usually chosen to have a horizontal line of sight, viewing the plasma perpendicularly from the low field side (LFS ECE) or from the high field side (HFS ECE). In these horizontal configurations, ECE measurements at the  $n$  harmonic take advantage of the  $1/R$  dependence of the electron cyclotron frequency [3],  $\omega_{nec} \sim neB(R)/m_e$ , to infer the radial profile of the electron temperature,  $T_e(R)$ . ECE has also been used to diagnose plasmas in which the electron distribution has departed from a Maxwellian distribution. For the diagnosis of non-thermal electrons, the vertical ECE configuration (V-ECE), with  $R$  constant along the line of sight, has proven to have the advantage of a more straightforward discrimination of the electron energy

<sup>5</sup> Present address: MIT—Plasma Science and Fusion Center, Cambridge, Massachusetts 02139, United States of America.

<sup>6</sup> See Reimerdes *et al* 2022 (<https://doi.org/10.1088/1741-4326/ac369b>) for the TCV Team.

\* Author to whom any correspondence should be addressed.



Original Content from this work may be used under the terms of the [Creative Commons Attribution 4.0 licence](https://creativecommons.org/licenses/by/4.0/). Any further distribution of this work must maintain attribution to the author(s) and the title of the work, journal citation and DOI.

according to the radiation frequency:

$$\omega \sim neB/\gamma m_{e0}, \quad (1)$$

where  $\gamma$  is the relativistic factor and  $m_{e0}$  is the electron rest mass ( $\gamma m_{e0} = m_e$ ).

The work presented in this paper, on the analysis of the electron energy distribution using V-ECE measurements, builds on previous works on Alcator C [4–9], TEXT-U [10, 11], WT-3 [12], DIII-D [13, 14], and PLT [15–17] tokamaks, which attempted to leverage the ideal one-to-one correspondence between measured frequency and electron energy in equation (1), by minimizing or mitigating issues such as harmonic overlap and multiple wall reflections. A method, described in [18], was also attempted to infer electron temperature from V-ECE measurements. In the following sections, we will discuss the experimental arrangement that enables the measurement of non-thermal electrons using V-ECE on the *Tokamak à Configuration Variable* (TCV) (section 2). The calibration of the diagnostic, which relies on V-ECE modeling and measurements free of background radiation, will be presented in section 3. V-ECE measurements of fast electron radiation in runaway electron scenarios and with Electron Cyclotron Current Drive (ECCD) will be discussed in section 4. The analysis of the electron energy distribution based on these measurements is presented in section 5, followed by the general conclusion of the paper. All physical quantities in this paper are expressed using the international system of units (SI). The angular frequency  $\omega$  in  $\text{rad s}^{-1}$  will be preferred for equations, while the frequency  $f$  in Hz will be used in quantitative assessments for practical reasons.

## 2. Experimental setup

The measurements discussed in this paper are carried out using the V-ECE diagnostic [19], installed on the TCV tokamak [20]. The diagnostic is equipped with a set of heterodyne radiometers measuring in the frequency range 78–114 GHz, with temporal resolution in the order of  $10 \mu\text{s}$  and bandwidth  $\sim 750 \text{ MHz}$ . The radiometer, described in detail in [21], is composed of three main stages: a radio frequency (RF) stage, an intermediate frequency (IF) stage, and a video stage. The incoming radiation from the plasma is split into the X- and O- polarization (X- and O-mode) using a wire grid polarizer, then downshifted to lower frequencies in the RF stage. This frequency conversion occurs in a mixer, which is a diode with a non-linear  $I/V$  characteristic. The lower frequency signals are amplified in the IF stage, rectified by a square-law diode detector, and further processed in the video stage, where the signals are amplified and low-pass filtered down to 100 kHz for acquisition. The optics of the diagnostic is arranged such that the vertical antenna pattern forms a Gaussian beam of waist radius  $\sim 3 \text{ cm}$  near the vessel mid-plane. In vacuum, the antenna pattern terminates, at the bottom of the machine, on a highly absorbing viewing dump [22], see figure 1(a). During plasma discharges, the antenna pattern can be shifted away

from the viewing dump, due to refraction, at a threshold electron density close to  $1 \times 10^{19} \text{ m}^{-3}$  [21]. The diagnostic measures fast electron emission at downshifted third or fourth harmonic emission as shown in figure 1(b). The electron energy that can be measured at each frequency is calculated in [19]. It is calculated that the maximum energy the diagnostic can measure without harmonic overlap is in the order of  $\sim 250 \text{ keV}$ . The ECCD experiments discussed in this paper exploit the X2 gyrotrons from the ECH, Electron Cyclotron Heating system on TCV [23]. The gyrotrons produce a wave at 82.7 GHz and nominal power  $\sim 680 \text{ kW}$ . The gyrotrons are connected to a launcher which direct the beam into the plasma. Current drive is achieved by imparting a parallel component, with respect to the plasma magnetic field, to the ECH wave vector. The location of the beam power deposition along the radial coordinate is generally controlled by the chosen value of magnetic field strength. The toroidal and poloidal directions of the beam (in the reference frame of the plasma) are controlled by the launcher angles, so-called launcher toroidal angle,  $\phi_L$ , and poloidal angle,  $\theta_L$  that can be varied during discharges.

## 3. Calibration

### 3.1. Background

The calibration of ECE diagnostics generally consists in determining, with the highest accuracy, the spectral response of the system to a given radiation power. Traditionally, two approaches have been retained for ECE calibration: (1) the use of sources of known characteristics as substitutes for the plasma and (2) the cross-calibration on a different, absolutely calibrated instrument. In the first approach, hot and cold sources are positioned within the vacuum chamber to irradiate the ECE antenna [24, 25]. The approach has been successfully employed since the 1970s in the vast majority of ECE systems in magnetic confinement devices, as demonstrated, for example, in [26]. A limitation of this approach in the past was that the calibration needed to be conducted inside the vacuum vessel, necessarily during a machine vent. The system's response, determined during a hot/cold source calibration, was typically used for several months, or even years, until the next calibration was feasible. This raised the question of the calibration's stability in relation to variations in experimental conditions, which could occur on a daily basis. The limitations of the calibration with a reference source inside the vacuum vessel have been addressed in previous works, such as in [27] by using external replica systems of ECE antennas, an application which is believed to be useful for ITER. The latter calibration approach exploits the absolute calibration of a different instrument within the same tokamak, to obtain the response function of an ECE system. The ECE system can be cross-calibrated on another ECE system as in JET [28], or can be cross-calibrated on a different diagnostic which measures the same plasma parameters such as Thomson Scattering (TS), inheriting all the uncertainties from the absolute calibration. This calibration method relies on the assumption

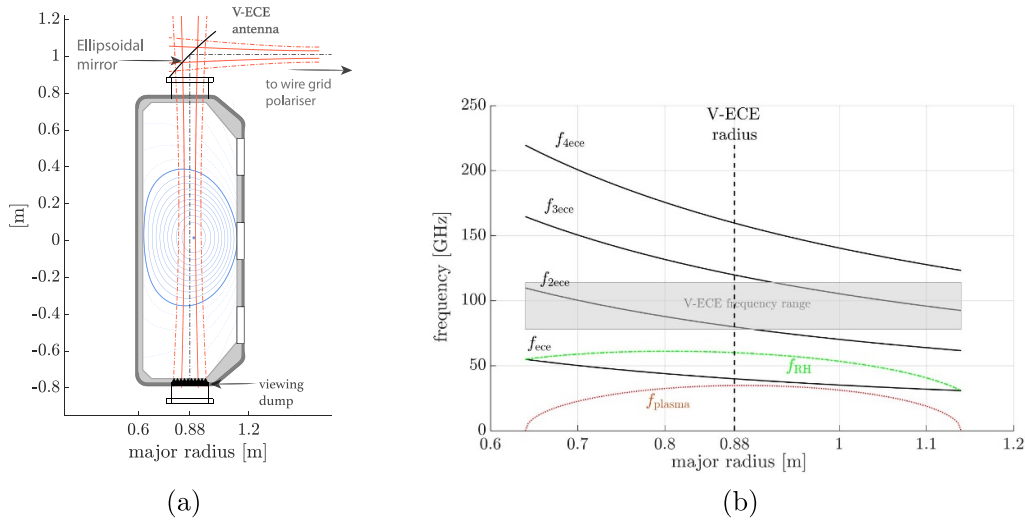


**Figure 1.** (a) V-ECE optics on TCv. The line of sight, which terminates on a beam dump (dark component below the machine floor) forms a Gaussian beam of radius  $\sim 3$  cm near the mid-plane. The radiation is reflected on an ellipsoidal mirror, split into X- and O- polarizations before detection in a heterodyne radiometer. (b) V-ECE frequency range, ECE harmonic frequencies ( $f_{nece}$ ), and right-hand cut-off frequency ( $f_{RH}$ ) on TCv with a toroidal magnetic field  $B_0 = 1.42$  T at the vacuum vessel center  $R_0 = 0.88$  m. The represented plasma frequency is computed with a central electron density of  $1.5 \times 10^{19} \text{ m}^{-3}$ .

that both diagnostics measure the same electron temperature. For ECE diagnostic systems, the measurement of the electron temperature requires that the plasma is optically thick and that the electron distribution is Maxwellian. When these conditions are fulfilled, successful cross-calibration of ECE systems with TS can be achieved, as demonstrated over the years, on TCv for example [29–33]. Historically, ECE and TS cross-calibration have used ohmic plasma discharges, which provide the best experimental plasma conditions allowing the assumption of a Maxwellian electron distribution. In other experimental conditions, such as those with Neutral Beam Heating (NBH) or Ion Cyclotron Resonance Heating (ICRH), discrepancies between ECE and TS can occur, and modeling of the electron distribution is required [34, 35]. For a vertical ECE configuration, a direct cross-calibration with TS cannot be achieved for two main reasons. First, even in an optically thick plasma, the radiation intensity measured with a vertical line of sight cannot be straightforwardly associated with a local electron temperature, since the ECE resonance is not well localized in the vertical direction. Second, the plasma is not usually optically thick for a vertical ECE line of sight above a certain frequency (approximately 86 GHz on TCv). At these higher, optically thin frequencies, an accurate estimation of the absorption coefficient and, consequently, the radiation intensity needs to be performed in order to use the plasma emission for calibration. Examples of calculations of radiation intensity in optically thin conditions have been reported in previous works, such as in DIII-D for the measurement of the electron temperature from the optically gray third harmonic [36], and in JET for calibrating the optically thin O1 (first harmonic O-mode) radiation for temperature measurement in the inboard (high field side) pedestal [37]. In both cases, a horizontal line of sight was employed.

### 3.2. Theory

The ECE spectral intensity  $I_\omega$  [38], for a radiation path in the plasma of total length  $L$  is expressed as

$$I_\omega = \hat{I}_\omega^{\text{inc}} e^{-\tau_0} + \frac{\omega^2}{8\pi^3 c^2} \int_0^L T_e(s) \alpha_\omega(s) e^{-\tau(s)} ds, \quad (2)$$

where the coordinate  $s$  measures the ray path along the plasma and  $\tau_0$  is the total plasma optical depth. The absorption coefficient,  $\alpha_\omega$ , represents the rate of absorption of the radiation per unit path length while  $T_e(s)$  stands for the temperature of the radiating electrons along the ray path. The first term in equation (2) represents the contribution of the incident radiation to the intensity, for example that of the thermal background radiation. It vanishes in case of no incident radiation,  $\hat{I}_\omega^{\text{inc}} = 0$ , or optical thick conditions  $\tau_0 \gg 1$ . In case of optically thin plasmas,  $\tau_0 < 1$ , an estimation of the contribution from multiple wall reflection is needed to assess  $\hat{I}_\omega^{\text{inc}}$ . That contribution can be neglected if the line of sight avoids radiation from multiple wall reflections, with a viewing dump as an example. If the electron distribution is Maxwellian and the plasma is optically thick ( $\tau_0 \gg 1$ ), the ECE radiation intensity is simply proportional to a local electron temperature and straight cross-calibration against, say, TS temperature can be achieved. In optically thin conditions and vertical-viewing line of sight, the intensity,  $I_\omega$  needs to be accurately estimated, by calculating the absorption coefficient [3, 39] along the ray trajectory, e.g. with the ray-tracing code SPECE [40], which solves the fully relativistic dispersion relation for EC waves. Experimentally, it is necessary to avoid incident radiation from multiple wall reflections for the accuracy of the calibration.

### 3.3. Measurement

The calibration uses measurements from thermal plasmas on TCv. During the plasma discharge the magnetic field is varied (ramped down and up), to identify the spectral features of the radiation. The variation of the magnetic field strength also allows the identification of several ECE resonances, meaning that multiple channels can be calibrated within a single discharge. The measurement in figure 2 shows X-mode intensity taken during TCv discharge #67946, in the frequency range 104–114 GHz. The magnetic field is ramped down from  $\sim 1.4$  T to  $\sim 1$  T and up again, while the plasma current remains nearly constant. Peaks are observed, consecutively in each channel during the field ramps. The peaks are symmetric and separated by a period during which the signal intensity is beneath the noise level of the radiometer. We observe approximately the same signal level for the peaks during the ramp down and the ramp up of the field. The intensity at the magnetic field flat-top is higher for the lowest frequencies during the first flat-top. In the second flat-top, at the end of the discharge, the lower signal level can be attributed to a drop in plasma optical depth due to reduced density. Figure 3 illustrates, for the frequency 108 GHz the spectral features of the measured signal. The two peaks in the signal are identified as single pass emission from the third harmonic. Radiation from multiple wall reflection, which originated as an X3 emission, is below noise level in between the two peaks. The radiation from multiple wall reflections, which originated as an X2 emission is observed outside the peaks. The diagnostic measures both reflected radiation and single pass radiation as the magnetic field is varied. When present, the reflected X2 radiation largely dominates the background contribution to the measurement. When the magnetic field is lower than the range in which the single pass X3 emissions is detected, the signal intensity drops to below the noise level confirming the absence of the background radiation originating as an X3 emission. We are certain that the reflected thermal X2 radiation cannot pollute the single pass X3 emission because the X2 cold resonance location is out of the plasma when that of the X3 traverses the line of sight. These observations suggest that the calibration can rely on modeling of only single pass X3 radiation measured by the radiometer.

We note that the lowest frequencies of the diagnostic can, in a single discharge, detect the single pass emission from both X2 and X3 (figure 4). The single pass X2 radiation, which is optically thick and reaches the black-body level whose intensity depends solely on the electron temperature. For this reason, X2 single pass measurement can be used to verify modeling of X3 V-ECE radiation.

### 3.4. Analysis

The modeling aims at providing an estimation of the radiated thermal power in each frequency bandwidth. The modeled power represents the power leaving the plasma to ensure that all components from the antenna to the detection system are included in the calibration. The modeled intensity from

SPECE is the spectral intensity  $I_\omega$  in equation (2). Integration over the bandwidth, effective area of the antenna and solid angle is performed to obtain the power in each bandwidth. Since the antenna pattern is modeled in SPECE with a set of rays, the size of the ECE emitting layer in the plasma, relative to the antenna beam size was assessed by calculating the profile of the absorption coefficient with analytical expressions from [39]. The modeling is performed accounting for the fact that the X3 emission layer is narrower than the antenna beam width. An optimization process was undertaken to determine the optimal number of rays and other parameters of the model. A scan of the total number of rays suggested a minimum of 24 rays to achieve convergence of the mean spectral intensity. The number of rays used in this modeling is distributed in SPECE as seven concentric annular sets, with four rays in each set. Scans of the line of sight around the vertical direction showed that an inclination of approximately  $3^\circ$  toward the HFS would reproduce best the measurement. The beam size used in the model is determined by comparing the width of the X3 and X2 resonances as they pass through the beam optics. A beam size of 3 cm is found to match the width of the resonances, consistent with beam size measurements in [19]. For the calculation of the power in the bandwidth, the synthetic diagnostic computes and sums spectral intensities at discrete values of frequencies in each bandwidth. A scan of the frequency step  $\delta_f$  informed the choice of bandwidth discretization, indicating a minimum requirement of 15 frequencies per frequency band ( $\delta_f \sim 53$  MHz).

#### 3.4.1. Calculation of the peak power in a frequency band.

The X- mode spectral intensities calculated for frequencies 108 GHz during TCv discharge #67946 and 81 GHz during #67946 are shown in figures 5 and 6. The results show good qualitative agreement between the modeling of the single pass radiation and the measurement. The modeling well predicts the temporal extent of the two peaks in #67946. The modeling, as expected does not calculate the background radiation from multiple wall reflections. The trends of the observed X2 and X3 single pass emissions are qualitatively reproduced by modeling. The model captures the flat trend of the X2 single pass radiation towards the end of the discharge. The model also exhibits a drop in intensity at the beginning of the discharge consistent with the measured signal.

The calibration factors are obtained by matching the modeled peak power with the measured voltage. The spectral intensities calculated for a few frequencies during discharge #67946 are shown in figure 7 with their profile in each bandwidth. The parabolic shape of the intensity profile in the bandwidth justifies the need for optimization of the frequency step. The bandwidth power  $P_{BW}$ , the total power in each frequency channel, is calculated as:

$$P_{BW} = 2\pi \int df dA d\Omega_S I(f). \quad (3)$$

From antenna theory, it can be shown that under certain approximation [41], the product  $dA d\Omega_S$  is only a function



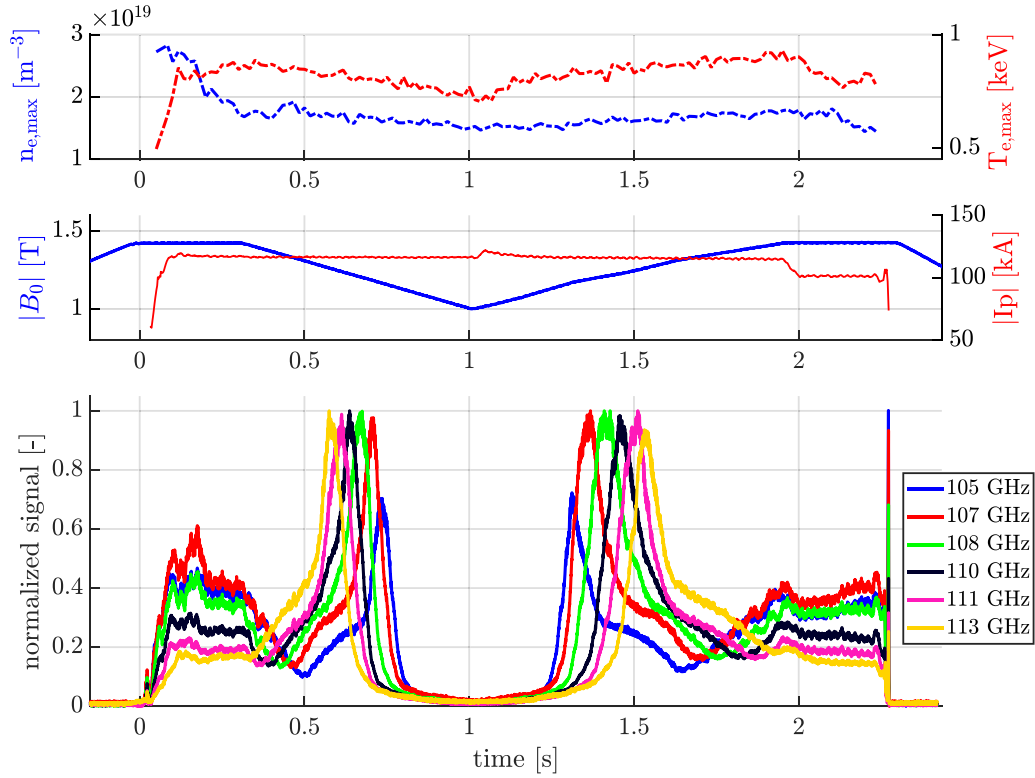


**Figure 2.** Measurement in the frequency range 104–114 GHz during the calibration discharge #67946 with two field ramps and flat plasma current.

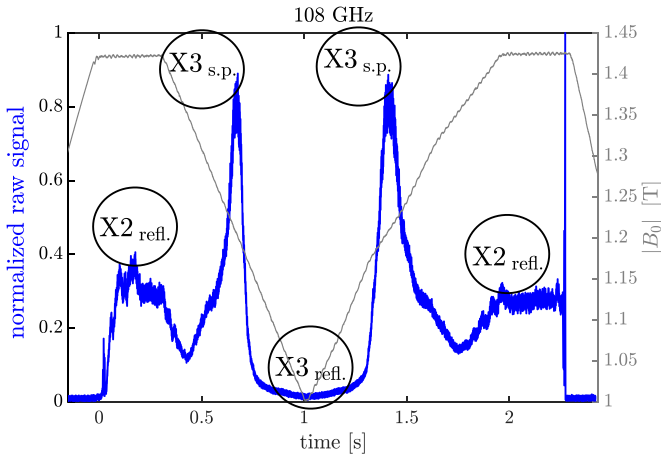


**Figure 3.** V-ECE signal measured at 108 GHz during TCV discharge #67946. The measurement shows single pass X3 radiation (X3 s.p.) and radiation from multiple wall reflections (X2 refl. and X3 refl.).

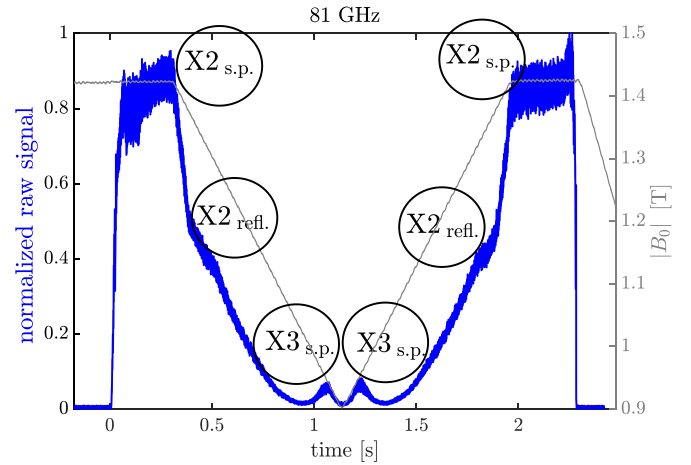


**Figure 4.** V-ECE signal at lower frequency (81 GHz) during TCV discharge #75022, showing detection of both X2 and X3 single pass radiation (X2 s.p. and X3 s.p.).

of the radiation wavelength,  $dA d\Omega_s \approx \lambda^2$ . Equation (3) thus reads

$$P_{\text{BW}} \approx 2\pi \int df \lambda^2 I(f) \approx 2\pi c^2 \int df \frac{I(f)}{f^2}. \quad (4)$$

### 3.5. Verification on the calibration

SPECE was used to estimate the bandwidth power. In an attempt to verify SPECE results on TCV, we first calculate

the radial profile of the radiation temperature as measured by LFS ECE. The modeling of the LFS ECE radiation intensity is consistent with expectations and is used as a sanity check of SPECE on TCV, see figure 8.

A verification of V-ECE calibration with SPECE is achieved with the plasma discharge #75022 in which the diagnostic measures both X2 and X3 single pass radiation, figures 4 and 6. The calibration factors, resulting from modeling of X3 intensity at  $\sim 1.1$  s and  $\sim 1.3$  s yield the intensity of

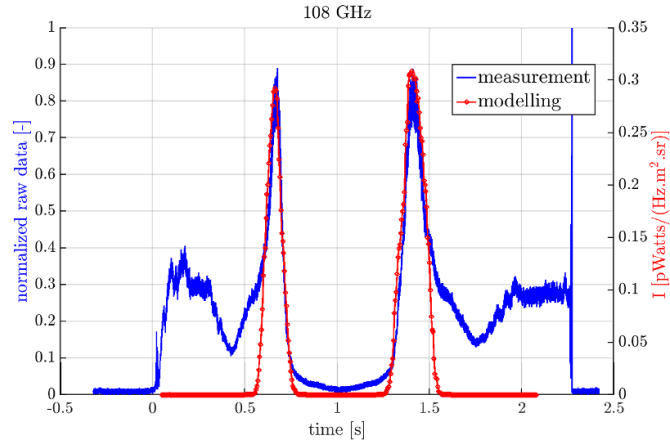


Figure 5. Modeling of the spectral intensity for the shot #67946 at frequency 108 GHz.

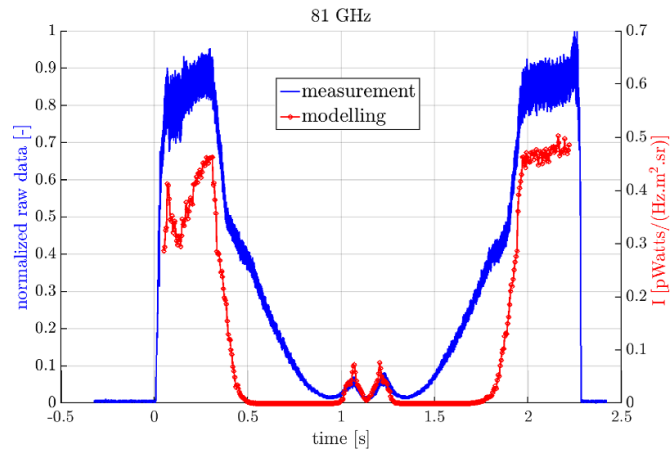


Figure 6. Modeling of the spectral intensity for the shot #75022 at frequency 81 GHz.

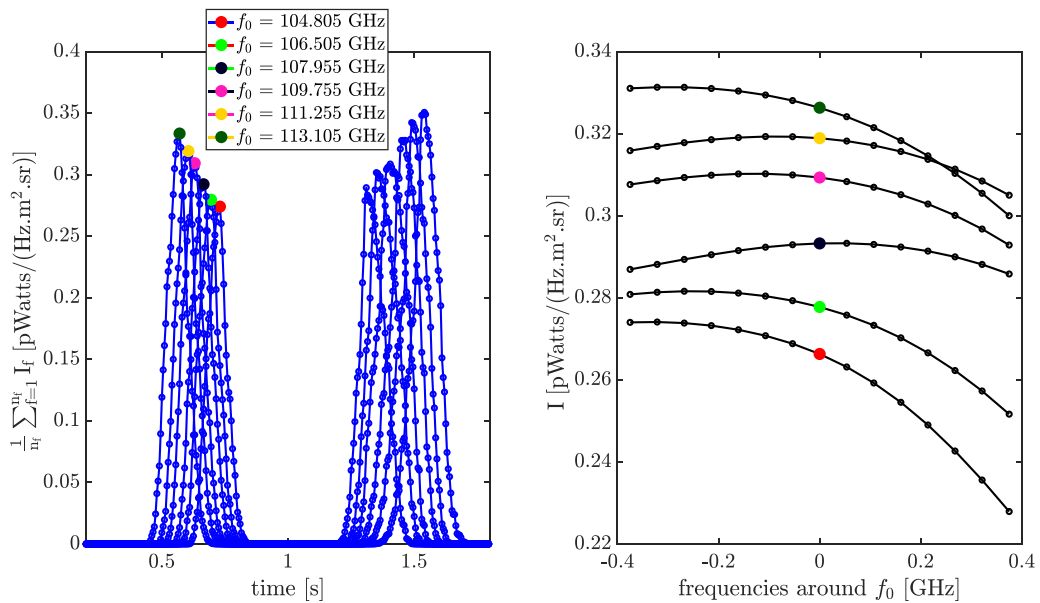
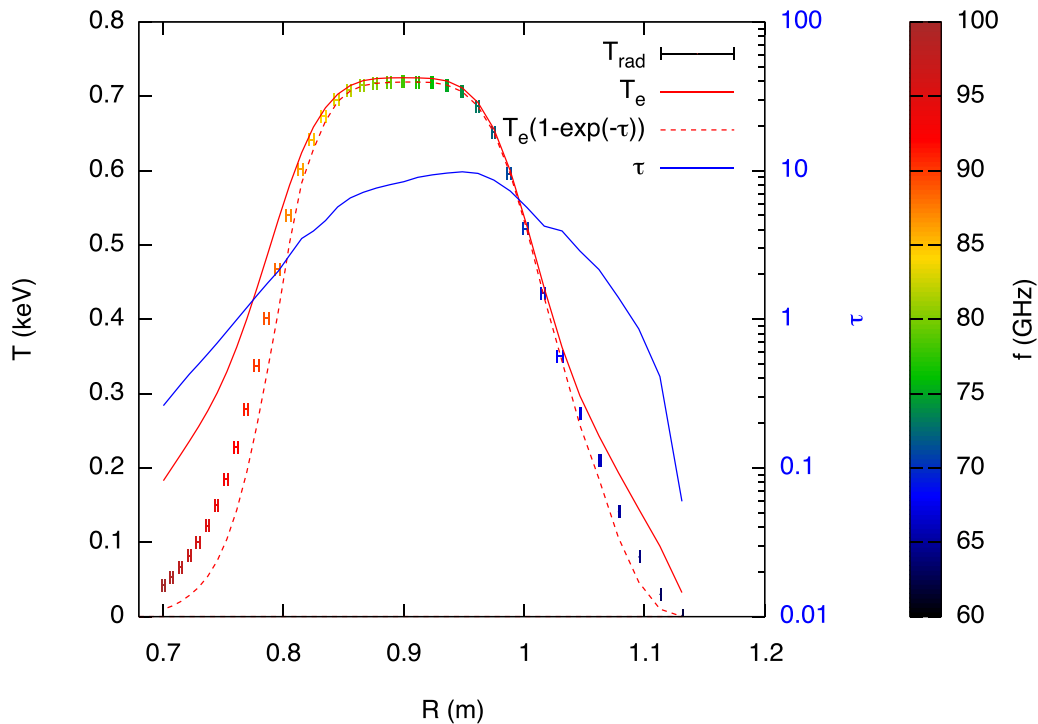


Figure 7. Modeled intensity in radiometer 104 – 114 GHz during the shot #67946.



**Figure 8.** A result of the synthetic diagnostic applied to a horizontal line of sight: the simulated antenna temperature ( $T_{rad}$ ) follows the antenna temperature as it is found analytically in a plasma with optical depth  $\tau \sim 1$ . In the tokamak center, the simulated radiation temperature coincides with the local electron temperature as expected in optically thick thermal plasmas.

the black-body power measured around 2 s (or around  $\sim 0.3$  s),  $P_{BB} \sim 94$  nW. The mean electron temperature associated with this black-body radiation is estimated as  $\bar{T}_e = P_{BB}/\Delta f_{BW} \sim 780$  [eV]. Value which is close to the central electron temperature of  $\sim 1$  keV measured in that plasma.

### 3.6. Discussing the uncertainties

The assessment of the uncertainty in the calibration factors is discussed for the case example of discharge #67946. The steps of the assessment are summarized in the diagram of figure 9. The steps are subdivided in two main branches. One branch for the uncertainty from the processing of the V-ECE raw signal. The other branch for the uncertainties in the estimation of the bandwidth power using the synthetic diagnostic.

The uncertainty in the V-ECE signal primarily arises from the digital (Butterworth) filtering of the raw data. Butterworth filtering is applied to the data to eliminate some noise in the detected signal, typically introduced by adjacent electronic components.

For the case of interest, the relative uncertainty on the filtered value used for the calibration is  $\delta_V/V < 5\%$ . To assess the uncertainty in the modeled bandwidth power, the uncertainties in the parameters are propagated from the raw measurement to the calculated bandwidth power, as shown in figure 9. The assessment does not account for the potential uncertainty in the measurement of the magnetic field because the diagnostic is calibrated with thermal peak measurement, when the resonance is within the line of sight. The measured frequencies and the line of sight constrain the value of

the magnetic field at the resonance. The uncertainties that are propagated are those from the measurement of the electron density,  $\delta_{n_e}$  and electron temperature,  $\delta_{T_e}$ . On TCVC, The relative errors for both density and temperature measurements with TS are respectively below 5% and 10% in the plasma center. Both values increase significantly at the plasma edge, up to 25% and 40% respectively. The high uncertainties on the density and temperature profiles at the edge do not impact significantly the modeled intensity. That is because the optical depth of the plasma drops at the edge in such a way that the intensity depends mainly on the parameters in the plasma center.

The relative uncertainty,  $\delta_I/I$ , on the computed spectral intensity for a frequency of 104 GHz is in the order of  $\delta_I/I < 25\%$ . Figure 10 shows the spectral intensities calculated with the synthetic diagnostic for different cases, with different uncertainties on the plasma profiles. The main contributor to the uncertainty on the spectral intensity is the uncertainty on the electron temperature. The uncertainty on the electron density plays a minor role. This is explained by the fact that the modeled radiation is single pass third harmonic intensity, which has a stronger dependence on the electron temperature.

Assuming that the relative uncertainties in the spectral intensity depend only on the plasma parameters and not on the modeled frequencies, the uncertainties in the spectral intensity will propagate unaffected through the integral of equation (4), giving an uncertainty on the modeled bandwidth power of  $\delta_P/P < 25\%$ . This sums up to an uncertainty on the calibration factor of the order of  $\delta_F/F < 30\%$ , accounting for the uncertainties in the modeled power and the uncertainties from the raw V-ECE signal. We note that this overall uncertainty on the



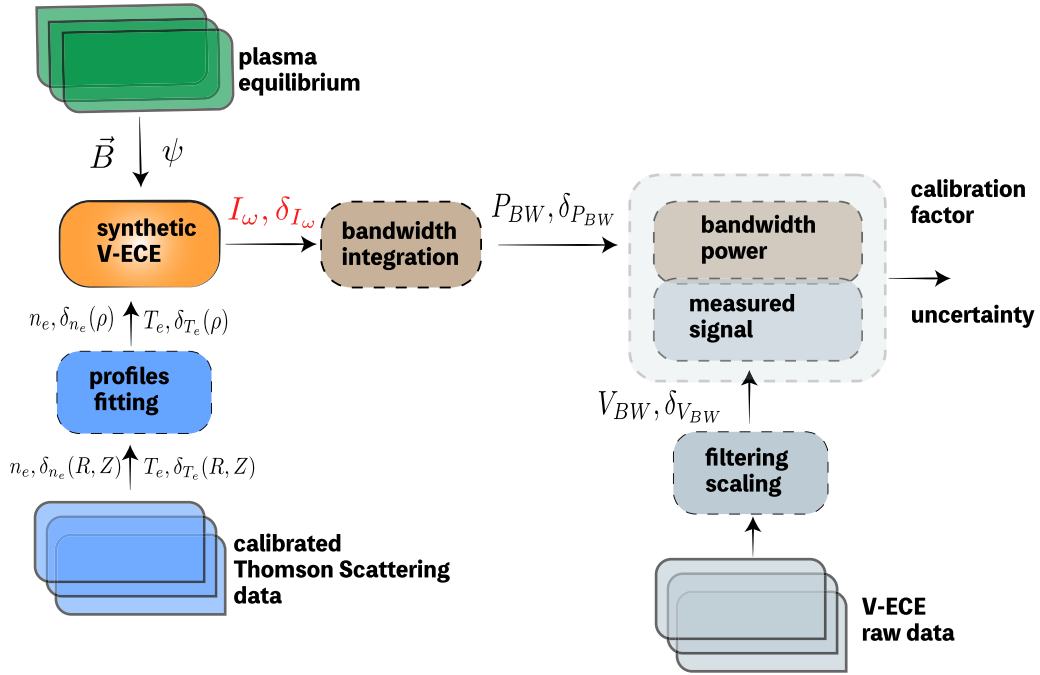


**Figure 9.** Block diagram illustrating the steps for the estimation of the uncertainty in the calibration procedure.

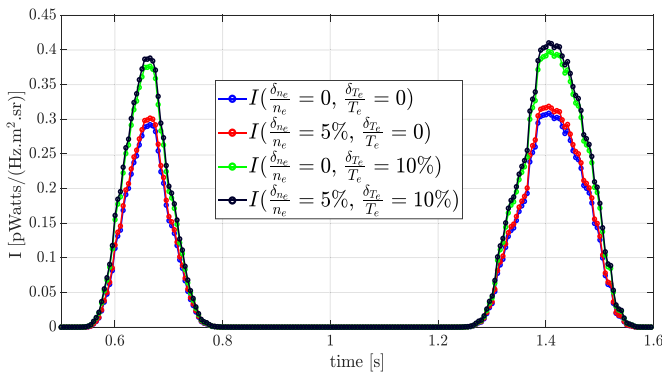


**Figure 10.** Spectral intensities calculated with plasma parameters affected by uncertainties.

calibration factor is essentially due to the systematic uncertainty on the raw electron temperature measured by the TS diagnostic.

## 4. Fast electron measurement

### 4.1. ECCD measurement

Calibrated V-ECE measurements during ECCD discharges #73217 and #72644 on TCV have been presented in [19]. Raw measurements during those discharges are shown in figure 11. Both discharges have similar values of ECH power. While the launcher toroidal angle is kept constant, the poloidal angle is varied in five steps during the heating phase between 0.7 s and 1.9 s in #72644. In this configuration, as the EC beam propagates along the plasma equatorial mid-plane, the launcher angle controls the parallel component of

the wave vector with respect to the toroidal magnetic field in the plasma. When this parallel wave-vector component is zero ( $\phi_L = 0$ ), the EC wave purely heats the plasma by increasing the perpendicular energy of the resonant electrons around a given parallel velocity. Increasing the parallel wave vector (by increasing  $\phi_L$ ) results in a Doppler shift of the EC resonance, pulling a suprathermal electron tail out of the bulk at higher velocities than the corresponding heating case [42]. The variation of the poloidal angle of the launcher from  $\sim 10^\circ$  to  $\sim 26^\circ$  in each step allows the observation of a stair-shaped X-mode radiation intensity. When no heating power is applied in either plasma discharge, the measured radiation has similar intensity levels in both discharges, corresponding to the thermal background radiation originating from X2 emission. As soon as the heating is turned on in the discharge #73217 at  $\sim 0.3$  s, all the channels immediately peak to reach a nearly stationary intensity level. We note how the intensity level during the discharge #73217 is generally higher than the intensity level in the discharge #72644 when the launcher configurations are similar. This is due to the more efficient current drive achieved in #73217, due in part to the lower density and higher electron temperature as the current drive efficiency is proportional, in general, to the ratio  $T_e/n_e$  [43]. When the heating is turned on during the discharge #72644, at  $\sim 0.7$  s, only the low energies ( $\sim 5$ – $26$  keV) exhibit a sharp jump in the measured intensity. The intensity at the higher energies ( $\sim 67$ – $75$  keV) shows a similar jump, with a delay of more than  $\sim 500$  ms, when the launcher angle has been moved to its third stage. From that moment, the dynamics is inverted and the higher energies now have the sharpest jump in intensity compared to the lower energies. Interestingly, the measurement at the middle energies, in our range, will then reach the highest value of intensity when the launcher angle reaches its last stage. In

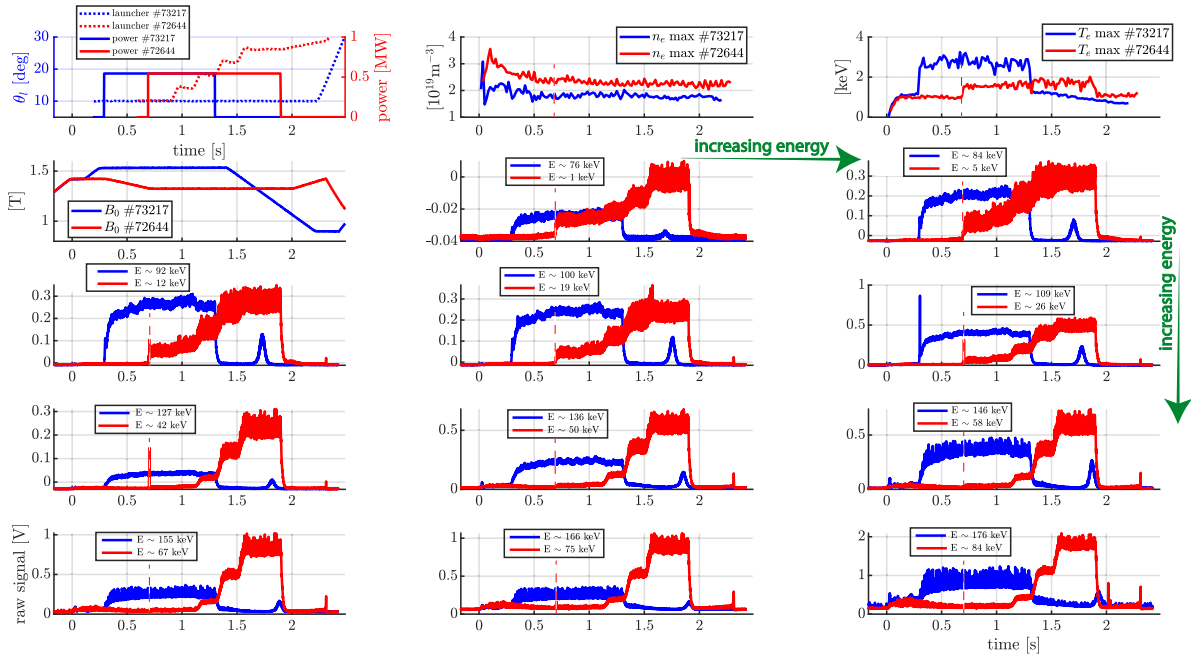


**Figure 11.** Raw measurements of X-mode intensity from discharges #73217 and #72644 in the frequency range of 96–114 GHz. The signals are plotted in decreasing frequency, from upper left to lower right. The energy measured at each frequency is calculated assuming a measurement of downshifted radiation from the third harmonic in both discharges. The subplot in the second row, second column, corresponds to the highest frequency and lowest energy (114 GHz,  $\sim 76$  keV in #73217 and  $\sim 1$  keV in #72644), while the subplot at the bottom right corresponds to the lowest frequency and highest energy (96 GHz,  $\sim 176$  keV in #73217 and  $\sim 84$  keV in #72644). The calculated energy differs between the two discharges due to the different values of magnetic field strength during the heating phase. The vertical dashed line represents the time when ECH starts in discharge #72644. The signal jump occurs farther from the vertical line at the highest energies.

measurements with Hard X-Ray tomographic Spectroscopy system (HXRS) [44] during the discharge #72644, the count rates shown in figure 12 allow similar observations on the effects of the launcher angle sweep. In TCV, hard x-rays are emitted by suprathermal electron bremsstrahlung and are measured between 20 and 200 keV with an 8 keV resolution. In figure 12, the sampling interval is set to 10 keV, which aligns with the resolution, making finer sampling unnecessary. Simulations of the ECH wave interaction with the plasma, for the discharge #72644 is achieved using the ray tracing code C3PO, solving the linear wave power absorption [45]. The refractive indices and the angle between the wave vector and the magnetic field, calculated at the wave absorption location for the various launcher angles are shown in table 1. The increase in the launcher poloidal angle allows to achieve higher values (in absolute terms) of the parallel refractive index. Higher parallel refractive indices generally allow the intersection between the EC resonant curves ( $v_{\perp}$  vs  $v_{\parallel}$ ) and the  $v_{\parallel}$  axis at higher values of  $v_{\parallel}$  [46], see figure 13. The physical mechanisms of the plasma-wave interaction mechanisms include, in general, momentum diffusion and pitch-angle scattering, which make the ECCD resonant interaction region complex to determine. For the purposes of this experiment it is observed that higher values  $\theta_L$  and thus higher absolute values of  $N_{\parallel}$  induce more energetic electrons in the plasma, explaining the different jumps in the measured intensities.

Figure 14 show the jumps in intensity, relative to the thermal phase, measured at each frequency in the different stages of discharge #72644. The jump is obtained by dividing the intensity in each heated stage by the intensity in the thermal phase. It is seen how at relatively low parallel refractive index ( $|N_{\parallel}| = 0.22$ ), the highest frequencies (lowest energies) jump is the most important. As  $|N_{\parallel}|$  increases, an IF (intermediate energy as well), near 104 GHz shows the sharpest jumps. We note that V-ECE X-mode intensity in ideal conditions depends on the density of the non-thermal electrons in a given energy band. That is, the highest jump observed around 104 GHz, with increasing  $|N_{\parallel}|$  suggests an increase in the number density of non-thermal electrons at the corresponding energy. This does not necessarily mean that the ECH wave is damped on electrons whose V-ECE energies are measured at 104 GHz when the refractive index increases. The increase of the number density at the given energy, which explains the sharp jump, is a consequence of the overall dynamics in the electron energy space, originally caused by the ECH wave. First-principle calculation using the code LUKE is used compute the electron energy distribution at the different stages of discharge #72644. The first calculation is shown in figure 15(a). The total number of electrons above a certain energy is plotted for a Maxwellian distribution and for the computed distribution. At a given energy, say 15 keV, which is above the electron thermal energy, the total number of electrons above that energy increases over time intervals (with

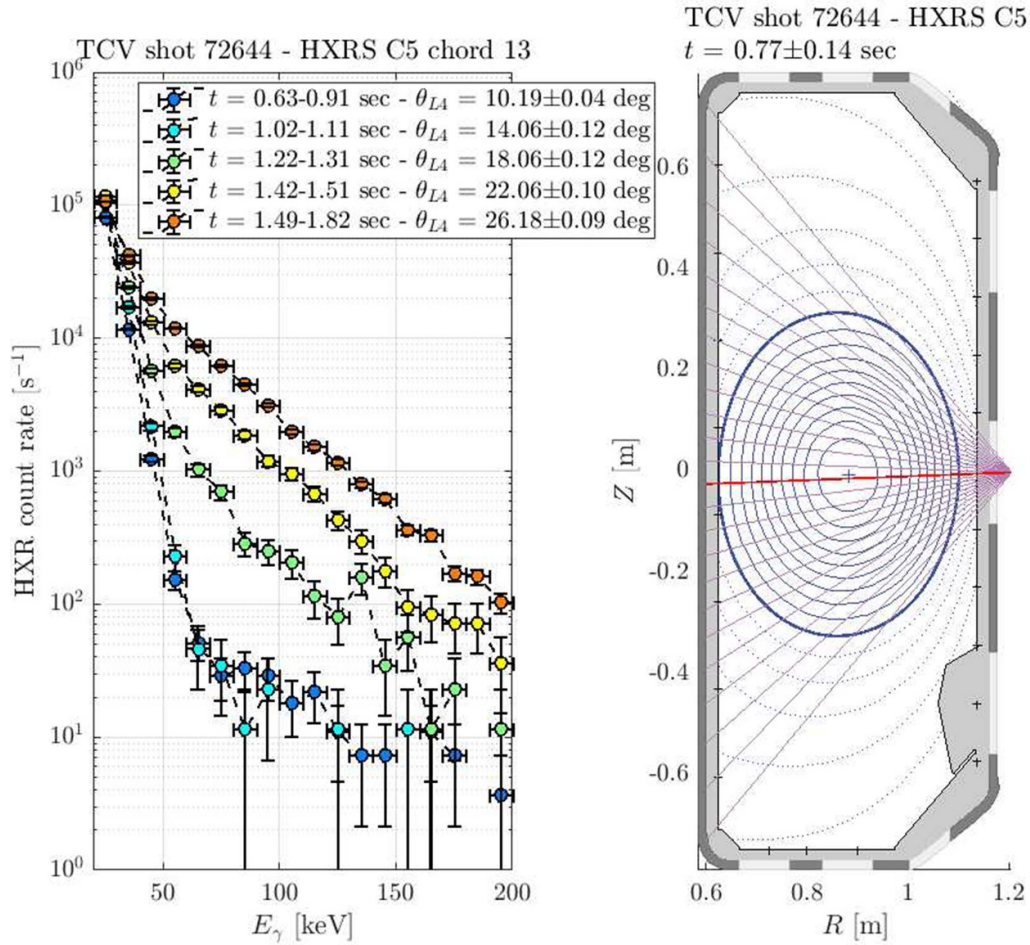


**Figure 12.** Hard-x-ray data for TCV discharge #72644, showing the effect of the change in the launcher poloidal angle. Higher count rates are measured at higher energies for increasing launcher poloidal angles.

**Table 1.** Summary of ECH parameters during TCV discharge #72644.

Launcher $\phi_l$ [°]	-90	-90	-90	-90	-90
Launcher $\theta_l$ [°]	10	14	18	22	26
$N_{  }$	-0.22	-0.31	-0.41	-0.51	-0.61
$\angle(\mathbf{k}, \mathbf{B})$ [°]	-16.7	-24.1	-33.05	-43.3	-55.1

increasing  $|N_{||}|$ ). This results confirms that low-energy electrons are pushed into the fast-electrons tail with ECCD and the number of transported electrons increases with parallel refractive index. Figure 15(b) shows the derivative of the number of electrons in the modeled distribution deduced from the density in the Maxwellian distribution. The discontinuity in the spectra is due to the logarithmic scale and to the absolute value in the plotted quantity. It represents the regions where the density in the Maxwellian distribution changes from higher to lower than that of the modeled distribution, which is the region in the phase space where the electrons are being pumped out by the ECH wave.

#### 4.2. Runaway electron measurement

X-mode measurement in the frequency range 78–96 GHz during runaway electron discharge #73002 on TCV is presented in figure 16. A thermal plasma discharge is run after the runaway experiment, with the optimal diagnostic setup, and is used for calibration of the diagnostic. The generation of runaway electrons is achieved by reducing the electron density at a plasma current  $\sim 150$  kA. The runaway electron beam was generated at around  $\sim 0.5$  s. The measurement shows a thermal phase before  $\sim 0.5$  s. The energies at which the thermal contribution is detected are associated to the lower frequencies, which have their X2 cold resonances within the

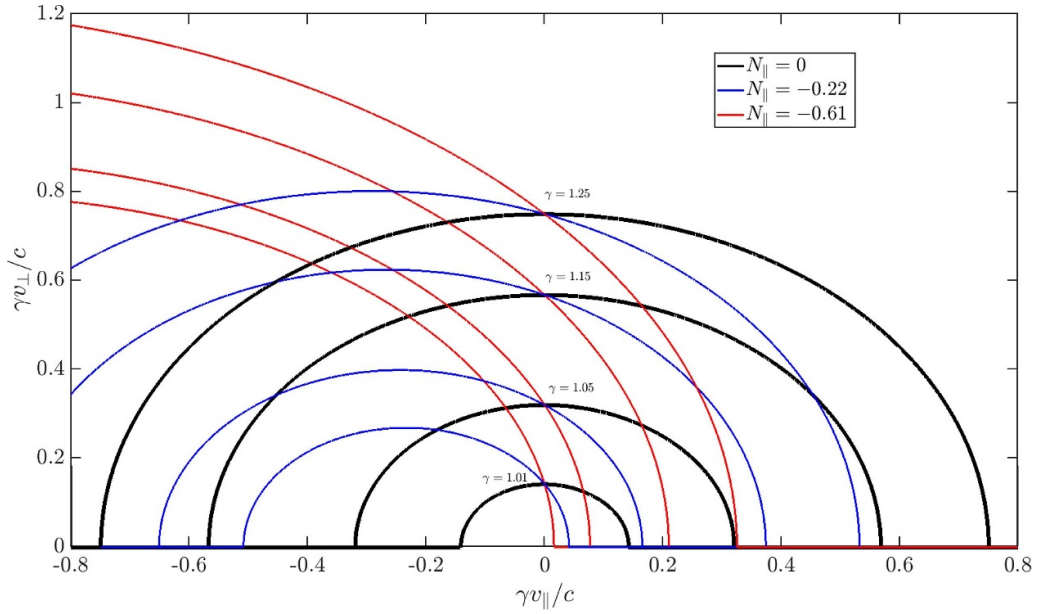


**Figure 13.** Electron cyclotron resonance curves for different values of parallel refractive index and energies.

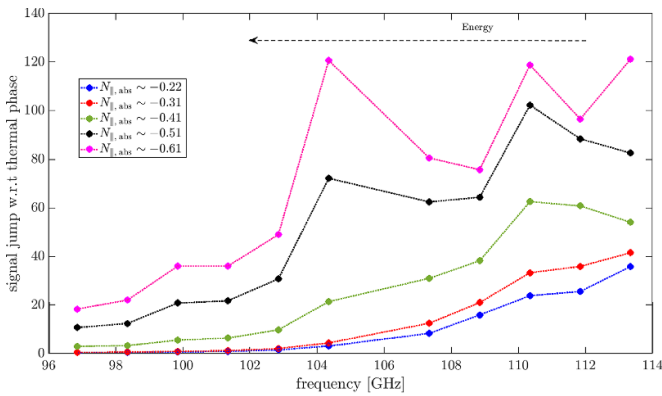


**Figure 14.** X-mode intensity as a function of energy at different values of parallel refractive index.

line of sight. The higher frequencies, which correspond to energies  $\sim 153$  keV in figure 16, have a smaller thermal contribution since their X2 thermal resonances are not within the line of sight. That is, from  $\sim 0.5$  s, the runaway electron radiation is measured by the diagnostic without thermal pollution from about  $\sim 0.5$  s at some of the energies. Moreover, the drop in the plasma density and temperature should reduce the thermal emission from 0.5 s at all energies. Finally, note that the flat ECE intensity after 0.5 s is not related to a saturation of the diagnostic. The runaway electron phase produces nearly constant intensity at V-ECE frequencies.

## 5. Analysis of the energy distribution

### 5.1. Theory of V-ECE measured distributions

By neglecting collective effects in the plasma, we aim to provide an expression of fast electron density at each energy (frequency) measured by V-ECE. The expression is found

assuming a two-parameters delta-type model distribution function, which is appropriate for V-ECE that measures simultaneously two independent quantities (X- and O- mode power) at the same frequency. We start from the expressions of the single particle emissivities [38], written for the O-mode as

$$\eta_O = \frac{e^2 \omega^2}{8\pi^3 \epsilon_0 c} \sum_{n=1}^{\infty} \left[ \frac{p^2 \cos^2 \theta_p}{1 + p^2} \mathcal{J}_n^2 \left( \frac{\omega}{\omega_{ece}} p \sin \theta_p \right) \right] \quad (5)$$

and for the X-mode as

$$\eta_X = \frac{e^2 \omega^2}{8\pi^3 \epsilon_0 c} \sum_{n=1}^{\infty} \left[ \frac{p^2 \sin^2 \theta_p}{1 + p^2} \mathcal{J}_n'^2 \left( \frac{\omega}{\omega_{ece}} p \sin \theta_p \right) \right], \quad (6)$$

where  $p$  is the normalized relativistic momentum,  $p = \gamma v/c$ , and  $\theta_p$  the pitch angle defined such that  $\sin(\theta_p) = v_{\parallel}/v$ .  $\mathcal{J}_n$  and  $\mathcal{J}_n'$  representing respectively the Bessel function of the  $n$  order and its derivative ( $n$  still representing the harmonic number). The X- and O-mode emission coefficients of an uncorrelated ensemble of electrons are expressed as

$$j_{O,X} = \int \eta_{O,X} \mathcal{F}(\vec{p}) d\vec{p}, \quad (7)$$

with  $\mathcal{F}$  representing the distribution function. The emitted power is calculated performing spectral and spatial integrals of the particle emissivity as well as an integration over solid angle  $\Omega_S$ . The spectral integration is performed in the frequency bandwidth around a given central frequency,  $\omega$ . The spatial integral is computed in the volume of plasma lying within the antenna pattern, estimated as the product of the effective area of the antenna  $A$ , in the radial direction, and the distance  $s$ , representing the vertical extent of the antenna:

$$P_{O,X}(\omega) = \int j_{O,X} ds dA d\Omega_S d\omega = \int \eta_{O,X} \mathcal{F}(\vec{p}) d\vec{p} ds dA d\Omega_S d\omega. \quad (8)$$

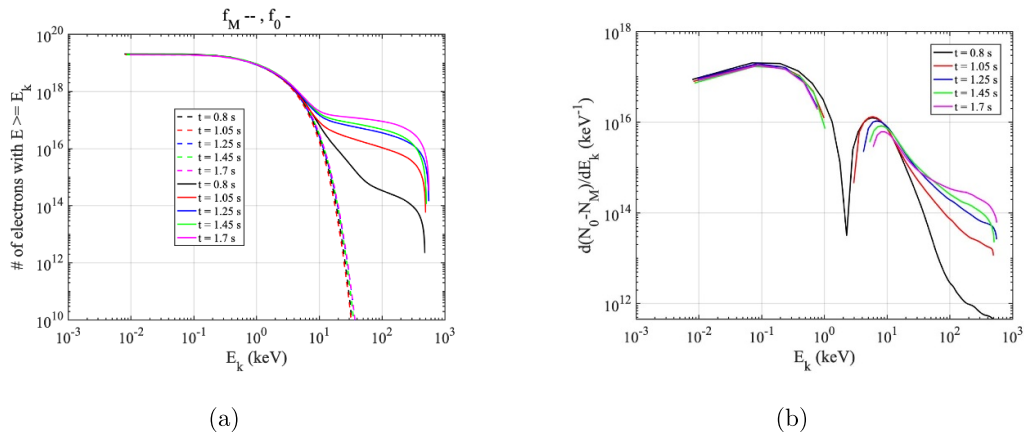


**Figure 15.** (a) Calculation with the code LUKE of the total number of electrons above a certain energy. The dashed lines are computed in the case of a Maxwellian distribution. The solid lines are obtained using the calculated non-thermal electron distribution in each phase of the ECCD discharge #72644. (b) Derivative with respect to energy of the number difference of electrons between the computed distribution and the Maxwellian distribution.

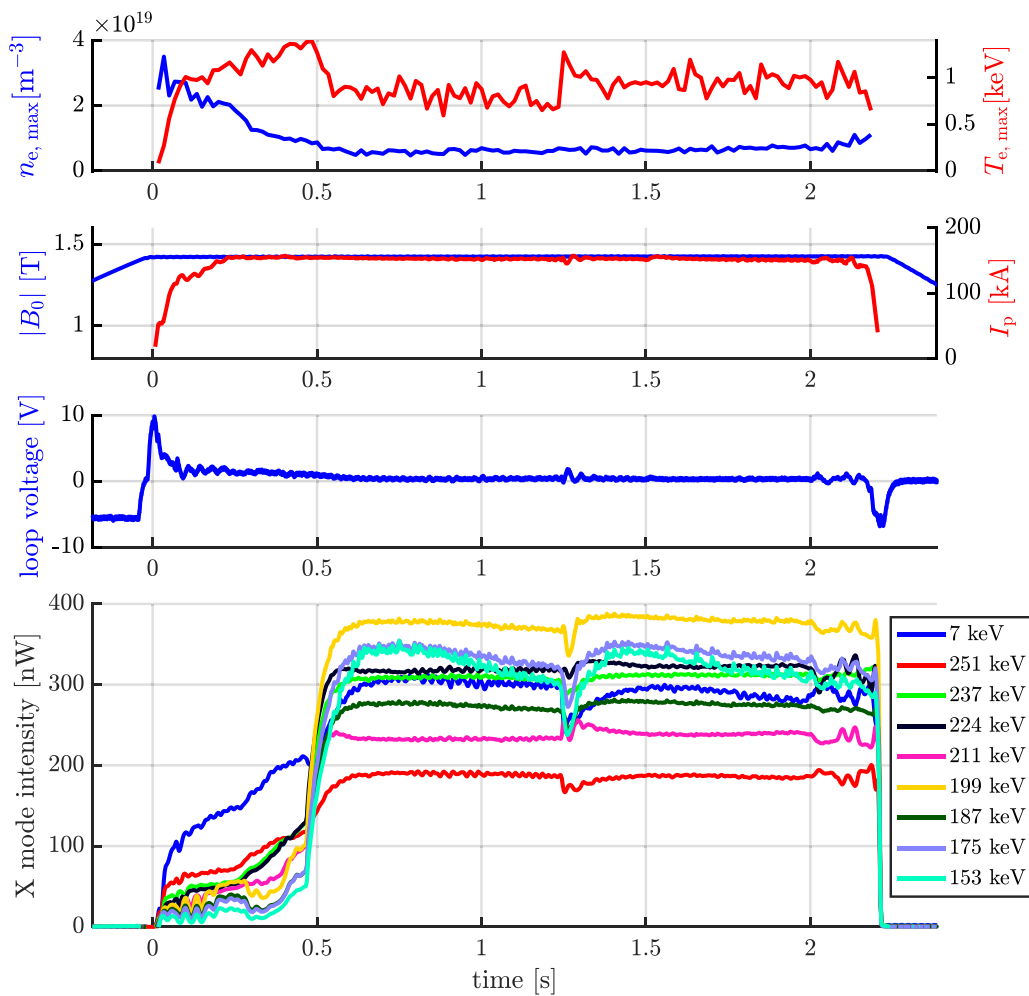


**Figure 16.** Time histories of V-ECE measurement in runaway electron discharge #73002 featuring typical plasma parameters plus measurements of X-mode radiation from the 78–96 GHz radiometer.



Previous methods to analyze the energy distribution based on V-ECE polarization measurements are reported in the literature [47]. We use the method introduced in [16], assuming a delta distribution of the form

$$\mathcal{F}(p_0, y) = \frac{n_{\text{fast}}}{2\pi p_0^2} \delta(p - p_0) \delta(y - y_0), \quad (9)$$

where  $y = \cos \theta_p$  and  $n_{\text{fast}}$  is the number density of fast electrons. The ratio  $j_X/j_O$  calculated in an appropriate coordinate system yields

$$\frac{j_X(\omega)}{j_O(\omega)} = \frac{1 - y_0^2}{y_0^2} \times \frac{\mathcal{J}_n'^2\left(\frac{\omega}{\omega_{\text{ece}}} p_0 \sqrt{1 - y_0^2}\right)}{\mathcal{J}_n^2\left(\frac{\omega}{\omega_{\text{ece}}} p_0 \sqrt{1 - y_0^2}\right)}. \quad (10)$$

The ratio determines directly a *weighted* pitch angle,  $y_0$ . Since the *weighted* pitch angle is obtained from the ratio of the emission coefficients prior to the integration, the inferred pitch angle and number density from measured power ratio represents an average over bandwidth and over plasma volume. The normalized momentum  $p_0$  is obtained directly from the measured frequency via the relation

$$p_0 = \sqrt{\left(\frac{n\omega_{\text{ece}}}{\omega}\right)^2 - 1}. \quad (11)$$

Figure 17 shows the ratios of the X- to the O-mode intensities computed using equation (10) for a range of energies (normalized momentum). The values of energies were found from the values of  $\omega_{\text{ece}}/10^9 \sim 2\pi \times 40 \text{ rad s}^{-1}$  ( $eB_0/m$  for  $B_0 = 1.41 \text{ T}$ ), and selected frequencies  $\omega$  in the range  $\omega \sim 2\pi \times [96\text{--}114] \text{ GHz}$ , corresponding to a V-ECE operational range. We note that the higher is the energy, the lower is the polarization ratio than can be achieved. This means that there is a minimum energy required to achieve a given ratio. The form of the curves, near the high values of  $y_0^2$ , is relatively flat, meaning that an uncertainty in the ratio can yield a large uncertainty on the *weighted* pitch angle. The assessment of the enhancement in the reconstructed distributions, in one of the directions, parallel or perpendicular to the field, is done by comparing the theoretical ratios in figure 17 to the measured ratio of intensities. Comparisons with an isotropic distribution can be made at each energy, in the different scenarios to determine the direction of the enhancement of the distribution. At a fixed energy, the lower ratios would suggest an enhancement in the parallel direction while the higher ratios would suggest an enhancement in the perpendicular direction.

The number density of fast electrons is estimated from the calibrated intensity measured in any of the polarizations. With X-polarization, the expression of the emitted power within a frequency bandwidth is found computing the integral in equation (8), which yields

$$P_{\text{BW},X} = \frac{e^2 c \widetilde{H}_p \Delta f}{2\epsilon_0 \widetilde{f}} n_{\text{fast}} p_0 (1 - y_0^2) \mathcal{J}_n'^2\left(\frac{\widetilde{f}}{f_{\text{ece}}} p_0 \sqrt{1 - y_0^2}\right). \quad (12)$$

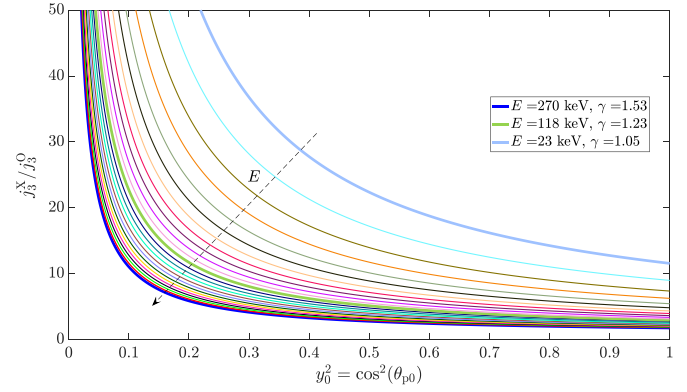


**Figure 17.** Calculated ratio of X- to O-mode intensities as a function of pitch angle at various energies.

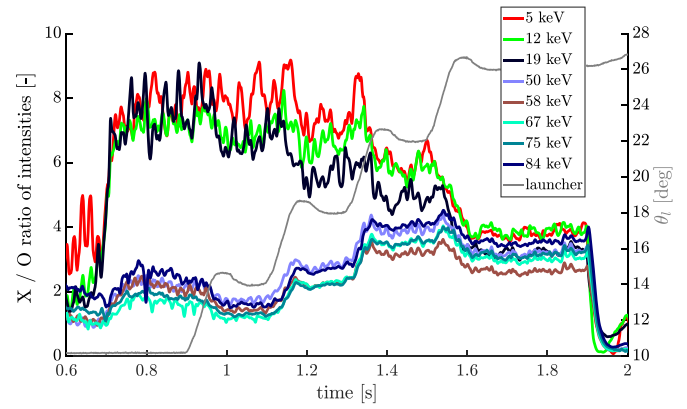


**Figure 18.** Measurement of polarization ratio for electron cyclotron current drive discharge #72644 on TCV.

The terms  $\widetilde{f}$  and  $\widetilde{H}_p$  represent respectively the mean frequency in the bandwidth and the mean plasma height within the antenna pattern. The number density of electrons at energy

$$E = \left(\frac{n f_{\text{ece}}}{\widetilde{f}} - 1\right) m_{e0} c^2, \quad (13)$$

measured from the  $n$  harmonic, in the channel centered at the frequency  $\widetilde{f}$  has the expression

$$n_{\text{fast}}(\widetilde{f}) = \frac{2\epsilon_0 \widetilde{f} P_{\text{BW},X}(\widetilde{f})}{e^2 c \widetilde{H}_p \Delta f p_0 (1 - y_0^2) \mathcal{J}_n'^2\left(\frac{\widetilde{f}}{f_{\text{ece}}} p_0 \sqrt{1 - y_0^2}\right)}. \quad (14)$$

## 5.2. Inferring the electron energy distribution from V-ECE measurements

The ratios of X- to O-mode intensities measured during the heating phase of the ECCD experiment #72644 are shown in figure 18. The O-mode intensities were measured using the same radiometer, in the frequency range 96–114 GHz, with a twin discharge (an exact repeat of discharge #72644), while the wire grid polarizer was rotated 90° in the plane parallel to



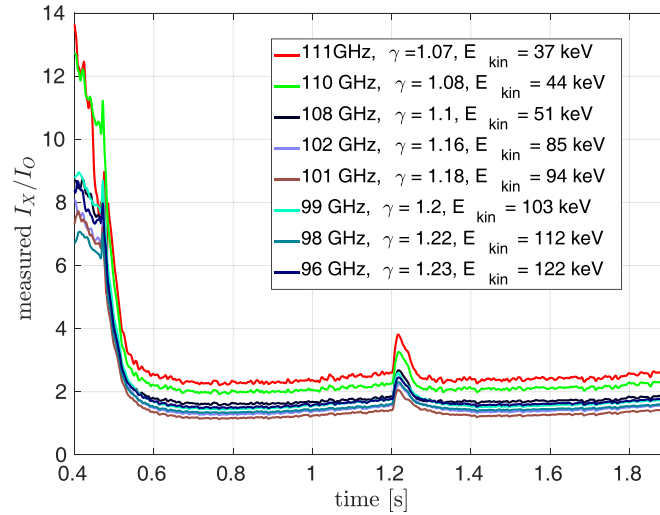


**Figure 19.** Measurement of the X- to O-mode radiation intensity ratio of the X-mode to for the runaway electron discharge.

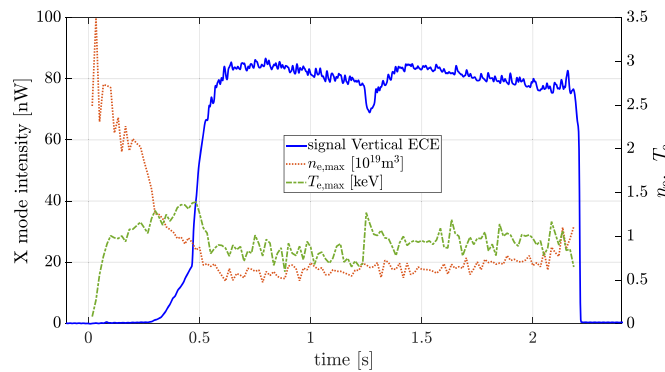


**Figure 20.** Runaway electron experiment used for the reconstruction of the non-thermal electron distribution. The figure shows a calibrated V-ECE signal together with electron density and temperature.

the grid. The energies are estimated, assuming harmonic overlap can be neglected, and that non-thermal contribution to the radiation comes essentially from the third harmonic emission.

For the lower energies, The ratio decreases with increasing  $\theta_L$ , suggesting that the parallel energy is been preferentially enhanced after the first launcher steps. This could mean that the interaction between the lower energy electrons and the ECH wave, which in principle enhances perpendicular energy, decreases with increasing  $|N_{||}|$ . In that case, the low energy electrons would have their energy enhanced from collisions with the higher energy electrons. The enhancement of the parallel energy through collisions may be responsible for the reduction of X- to O-mode power ratio. At the lower energies, the ratio is higher for smaller  $|N_{||}|$  and launcher angle  $\theta_L$ . This trend is inverted at the higher energies, where the polarization ratios have lower values in general. It is observed that small  $|N_{||}|$  leads to stronger enhancement in the perpendicular direction, explaining the higher ratio of the X- to the O- mode intensities. At higher  $|N_{||}|$  (approximately between 1.4s and 1.6s), the higher energies are more enhanced in the perpendicular direction, consistently with the expectations. The ratio of the intensities of the X- to the O-mode intensity for the runaway electron case #73002 is shown in figure 19.

The ratio sharply decreases when the runaway beam starts, confirming that it is the parallel energy of the electrons that is been enhanced, in particular due to the toroidal electric field acceleration. In general the ratio is lower for runaway electron radiation, at each measured frequency, compared to the suprathermal electrons generated by ECCD in the case presented in figure 18. Note that the discussed polarization ratios are free from the calibration uncertainties mentioned in section 3.6. The ratios are obtained from the radiometers' raw data, accounting for the radiometers' insertion losses. The insertion losses were determined by rotating the wire grid polarizer by  $45^\circ$  with the plasma as a source, and by using an external power source from a vector network analyzer.

We focus on the runaway electron experiment #73002 on TCV for the reconstruction of the energy distribution. That is for two main reasons. The first reason is that the ECCD experiment is performed at a much higher density and necessitates the inclusion of the collective effects. The second reason is because the approach using the polarization ratios may not be appropriate in the high density case, due to possible detection of radiation from multiple wall reflections, which will contaminates the ratio of polarization when plasma refraction is not mitigated. The polarization ratios in the ECCD case can be

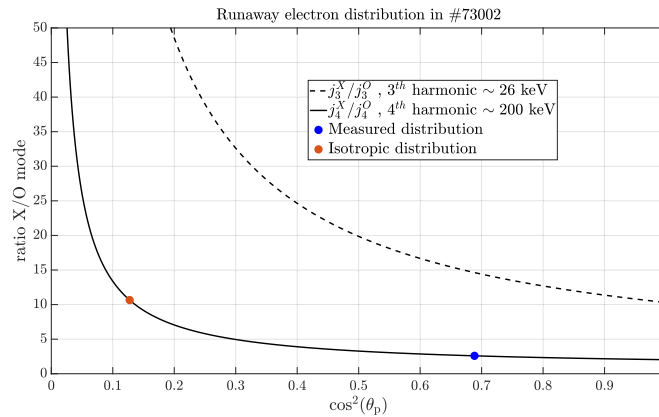


**Figure 21.** Polarization ratios of an isotropic distribution compared to the ratio from the runaway experiment.

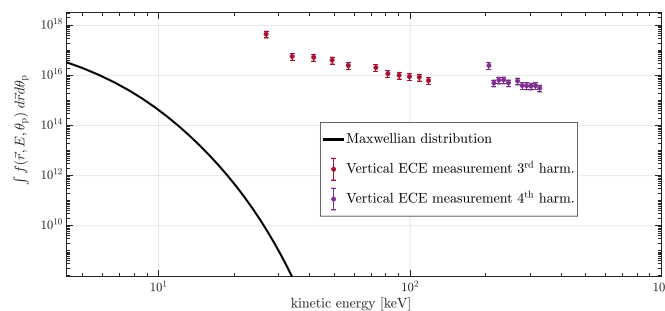


**Figure 22.** Example of reconstruction of the electron distribution in a runaway electron measurement with V-ECE using a 2-parameter model.

useful for identifying enhancements in the parallel/perpendicular energy. However, the absolute values of these ratios in ECCD should not be directly compared to those in the runaway case. The analysis in the runaway electron case is based on figure 20, where time traces of V-ECE signal central density and temperature are shown. The time of the runaway beam formation is identified around  $\sim 0.5$  s, and the ratio of intensities that is used is obtained after that time. The polarization ratio for a single channel is shown on figure 21. Assuming that the polarization ratio obtained in the runaway case is not contaminated, a much higher energy is needed in order to match the measured ratio, suggesting that the measured emission primarily comes from downshifted emission from the 4th harmonic and not from the above 3rd harmonic. With the emission coming from the 4th harmonic, the electron energy is sufficient to achieve the measured ratio of polarized intensities. In general, the emission that is detected comes from more than one harmonic. In the case of runaway electrons, the expected distribution is flat and, higher energy emission can actually dominate the total radiation. This analysis suggests a net enhancement in the parallel direction is observed for runaway electrons as expected with a value of *weighted* pitch angle close to  $y_0^2 \sim 0.68$ .

We compute the density of runaway electrons at measured energy using equation (14) and the calibrated X-mode intensities (shown for one channel on figure 20). We note that at the beginning of the discharge, before the runaway beam formation at  $\sim 0.5$  s, the measured power is null and so is the

number density of the runaway electrons. The calculated number density of runaway electrons at some energies, when the beam is formed, is shown in figure 22. The densities are compared to those of a Maxwellian distribution. We note that the numbers shown in the figure are the fast electron density found with equation (14) and multiplied by a plasma volume, to obtain a total number of particles at a given energy. The reconstructed energy distribution is shown for both assumptions that the measured radiation comes primarily from downshifted 3rd (lower energies) or downshifted 4th harmonic (higher energy). The relatively flat tail, and the large number of electrons present at that high energy in the reconstructed distribution, compared to a Maxwellian distribution, shows the possibility of using V-ECE measurement for runaway electron distribution studies with.

## 6. Conclusion

This paper presented the first V-ECE measurements of non-thermal electrons on TCX. The diagnostic more easily discriminates the radiation according to the energy of the electrons, compared to horizontally-viewing ECE diagnostics. The calibration of the diagnostic relied on the calculation of radiation intensity under the conditions of low optical thickness, and was verified using the plasma black-body radiation. Uncertainties in the calibration were found to lie below 30%. The main contributions to the error margin are the systematic

errors in the TS measurements of electron density and temperature profiles. Measurements of radiation from non-thermal electrons discharges were discussed. The measurements of linearly X- and O-polarized radiation were achieved in ECCD and runaway electron scenarios. The paper has described a scenario designed to combine calibration and current drive in a single plasma discharge. In an ECCD scenario with varying launcher angle, stair-shaped V-ECE measurements and HXRS measurements allowed to observe how increasingly energetic electrons are excited with increasingly higher absolute values of ECH wave  $N_{\parallel}$ . From V-ECE measurements, it was observed an energy region, measured at around 104 GHz, showing a significant excitation by the ECH wave for values of  $N_{\parallel} \sim -0.41, -0.51, \text{ and } -0.61$ . The observation suggested that electrons in that energy space preferentially receive the ECH wave energy due to the overall wave-plasma dynamics and not necessarily to the direct damping of wave on those electrons. V-ECE measurements in runaway electron scenarios has facilitated the analysis of the electron energy distribution. Ratios of X- to O- mode radiation intensities used in a two-parameters model for the energy distribution, has shown enhancement of the energy distribution in the parallel direction in runaway electron case, while enhancements in both parallel and perpendicular directions were found in ECCD case. Future work on TCV could include multi-diagnostic reconstruction of the electron energy distribution leveraging the advantages of V-ECE such as great temporal resolution and one-to-one correspondence between energy and measured frequency in ideal conditions.

The work described in this article displays important advancements over previously published results and has the potential to inspire future research on V-ECE diagnostics and calibration of ECE instruments. A key strength of this work is the interpretation of diagnostic results almost free from thermal background radiation. This achievement is made possible by better control over multiple wall reflections and represents an innovation compared to previous studies, where viewing dumps were considered *sine qua non* conditions for operating the diagnostic. The control of background radiation, demonstrated for the first time in this work has notably enabled a more accurate cross-calibration of V-ECE with TS. Techniques that allow regular calibration of ECE diagnostics without requiring machine venting will be beneficial for next-generation machines such as ITER, SPARC, or DEMO. More broadly, the results presented in this article could help revive interest in fast electron diagnostics in tokamaks using ECE. As demonstrated on TCV, V-ECE can play a key role in the detection and mitigation of low-energy runaway electrons, bringing us a step closer to achieving fusion energy.

### Data availability statement

All data that support the findings of this study are included within the article (and any supplementary files).

### Acknowledgments

The first author, A T B, thanks Olivier Sauter, Patrick Blanchard, Gerardo Giruzzi and Max Austin for their valuable insights. This work has been carried out within the framework of the EUROfusion Consortium, via the Euratom Research and Training Program (Grant Agreement No 101052200 - EUROfusion) and funded by the Swiss State Secretariat for Education, Research and Innovation (Staatssekretariat für Bildung, Forschung und Innovation—SBFI). Views and opinions expressed are however those of the author(s) only and do not necessarily reflect those of the European Union, the European Commission, or SBFI. Neither the European Union nor the European Commission nor SBFI can be held responsible for them. This work was supported in part by the Swiss National Science Foundation.

### ORCID iDs

A Tema Biwole  <https://orcid.org/0000-0002-4705-2743>  
 A Fasoli  <https://orcid.org/0000-0003-4319-5736>  
 L Figini  <https://orcid.org/0000-0002-0034-4028>  
 J Decker  <https://orcid.org/0000-0003-0220-2653>  
 M Hoppe  <https://orcid.org/0000-0003-3994-8977>  
 J Cazabonne  <https://orcid.org/0000-0001-7629-1375>  
 S Coda  <https://orcid.org/0000-0002-8010-4971>

### References

- [1] Hutchinson I H 2002 *Principles of Plasma Diagnostics* (Cambridge University Press)
- [2] Hartfuss H J and Geist T 2013 *Passive Diagnostics* (Wiley) ch 4, pp 117–50
- [3] Bornatici M, Cano R, De Barbieri O and Engelmann F 1983 Electron cyclotron emission and absorption in fusion plasmas *Nucl. Fusion* **23** 1153–257
- [4] Kato K and Hutchinson I H 1986 Nonthermal electron velocity distribution measured by electron cyclotron emission in alcator C Tokamak *Phys. Rev. Lett.* **56** 340–3
- [5] Hutchinson I H, Kato K and Texter S C 1986 Measurements of mildly relativistic electron distribution functions during lower hybrid heating and current drive (invited) *Rev. Sci. Instrum.* **57** 1951–5
- [6] Hutchinson I H and Kato K 1986 Diagnosis of mildly relativistic electron distributions by cyclotron emission *Nucl. Fusion* **26** 179–91
- [7] Kato K 1986 Diagnosis of mildly relativistic electron velocity distributions by electron cyclotron emission in the alcator C Tokamak *PhD Thesis* Massachusetts Institute of Technology
- [8] Kato K and Hutchinson I H 1986 Alcator C vertical viewing electron cyclotron emission diagnostic *Rev. Sci. Instrum.* **57** 1959–61
- [9] Kato K and Hutchinson I H 1987 Diagnosis of mildly relativistic electron velocity distributions by electron cyclotron emission in the alcator C Tokamak *Phys. Fluids* **30** 3809
- [10] Giruzzi G, Steimle R F, Roberts D R, Sing D and Wootton A J 1996 Identification and measurement of core plasma turbulence by observation of fast electrons in TEXT-U *Plasma Phys. Control. Fusion* **38** 1593–602

- [11] Roberts D R, Steimle R F, Giruzzi G, Cima G and Watts C 1995 Vertical viewing of electron-cyclotron emissions for diagnosing fast-electron dynamics in TEXT-U *Rev. Sci. Instrum.* **66** 427–9
- [12] Ide S et al 1989 Investigation of high energy electrons in lower hybrid current drive plasma with electron cyclotron emission measurement in the WT-3 tokamak *Nucl. Fusion* **29** 1325–38
- [13] James R, Janz S, Ellis R, Boyd D and Lohr J 1988 Vertical-viewing electron cyclotron emission diagnostic for the DIII-d tokamak *Rev. Sci. Instrum.* **59** 1611–3
- [14] Janz S J 1992 Analysis of nonthermal electron cyclotron emission during electron cyclotron current drive experiments on the DIII-D tokamak *PhD Thesis* University of Maryland
- [15] Luce T C Superthermal electron distribution measurements with electron cyclotron emission *PhD Thesis* Princeton University
- [16] Luce T C, Efthimion P C and Fisch N J 1988 Superthermal electron distribution measurements from polarized electron cyclotron emission (invited) *Rev. Sci. Instrum.* **59** 1593–8
- [17] Luce T C, Efthimion P C, Fisch N J, Bell R E and Stevens J E 1987 Modeling of vertical ECE during lower hybrid current drive on PLT *AIP Conf. Proc.*
- [18] Michelot Y, Segui J-L and Giruzzi G 1996 Electron temperature diagnostic in tokamak plasmas by microwave transmission *Nucl. Fusion* **36** 309–19
- [19] Tema Biwole A, Porte L, Coda S and Fasoli A 2023 Vertical electron cyclotron emission diagnostic on the tokamak à configuration variable *Rev. Sci. Instrum.* **94** 103504
- [20] Reimerdes H et al 2022 Overview of the TCV tokamak experimental programme *Nucl. Fusion* **62** 042018
- [21] Tema Biwole A 2023 Measuring the electron energy distribution in tokamak plasmas from polarized electron cyclotron radiation *PhD Thesis* Ecole Polytechnique Fédérale de Lausanne (<https://doi.org/10.5075/epfl-thesis-9882>)
- [22] Tema Biwole A, Porte L, Fasoli A, Simonetto A and D'Arcangelo O 2021 Performance of a high vacuum, high temperature compatible millimeter-range viewing dump for the vertical ECE experiment on TCV *Fusion Eng. Des.* **162** 112079
- [23] Paley J I et al 2009 Real time control of plasmas and ECRH systems on TCV *Nucl. Fusion* **49** 085017
- [24] Costley A E, Hastie R J, Paul J W M and Chamberlain J 1974 Electron cyclotron emission from a tokamak plasma: experiment and theory *Phys. Rev. Lett.* **33** 758–61
- [25] Costley A 2009 ECE: the story so far *Electron Cyclotron Emission and Electron Cyclotron Resonance Heating* (WORLD SCIENTIFIC) p EC-15
- [26] Buratti P and Zerbini M 1995 A Fourier transform spectrometer with fast scanning capability for tokamak plasma diagnostic *Rev. Sci. Instrum.* **66** 4208–17
- [27] Buratti P, Tudisco O and Zerbini M 1993 A broadband light collection system for ece diagnostics on the FTU tokamak *Infrared Phys.* **34** 533–41
- [28] Schmuck S, Fessey J, Gerbaud T, Alper B, Beurskens M N A, de la Luna E, Sirinelli A and Zerbini M 2012 Electron cyclotron emission measurements on JET: Michelson interferometer, new absolute calibration and determination of electron temperature *Rev. Sci. Instrum.* **83** 125101
- [29] Blanchard P, Alberti S, Coda S, Weisen H, Nikkola P and Klimanov I 2002 High field side measurements of non-thermal electron cyclotron emission on TCV plasmas with ECH and ECCD *Plasma Phys. Control. Fusion* **44** 2231–49
- [30] Blanchard P 2002 Etudes du rayonnement suprathermique emis lors du chauffage cyclotronique électronique du plasma du tokamak TCV *PhD Thesis* Ecole Polytechnique Fédérale de Lausanne
- [31] Klimanov I 2005 Reconstruction of the electron distribution function during ecrh/eccd and magnetic reconnection events in a tokamak plasma *PhD Thesis* Ecole Polytechnique Fédérale de Lausanne
- [32] Klimanov I, Porte L, Alberti S, Blanchard P, Fasoli A and Goodman T P 2005 Electron cyclotron emission spectrometry on the tokamak à configuration variable *Rev. Sci. Instrum.* **76** 093504
- [33] Fontana M, Porte L, Coda S and Sauter O 2017 The effect of triangularity on fluctuations in a tokamak plasma *Nucl. Fusion* **58** 024002
- [34] de la Luna E, Krivenski V, Giruzzi G, Gowers C, Prentice R, Travers J M and Zerbini M 2003 Impact of bulk non-Maxwellian electrons on electron temperature measurements (invited) *Rev. Sci. Instrum.* **74** 1414–20
- [35] Fontana M et al 2023 High  $T_e$  discrepancies between ECE and Thomson diagnostics in high-performance jet discharges *Phys. Plasmas* **30** 2023
- [36] Austin M E, Ellis R F, James R A and Luce T C 1996 Electron temperature measurements from optically gray third harmonic electron cyclotron emission in the DIII-D tokamak *Phys. Plasmas* **3** 3725–31
- [37] Barrera L et al 2010 Inboard and outboard electron temperature profile measurements in jet using ECE diagnostics *Plasma Phys. Control. Fusion* **52** 085010
- [38] Bekefi G 1966 *Radiation Processes in Plasmas* (Wiley)
- [39] Bornatici M 1982 Theory of electron cyclotron absorption of magnetized plasmas *Plasma Phys.* **24** 629–38
- [40] Farina D, Figini L, Platania P, Sozzi C, Gorini G, Orsitto F P, Sindoni E and Tardocchi M 2008 SPECE: a code for electron cyclotron emission in tokamaks *AIP Conf. Proc.* **988** 128–31
- [41] Shaw J A 2012 Radiometry and the Friis transmission equation *Am. J. Phys.* **81** 33–37
- [42] Prater R 2004 Heating and current drive by electron cyclotron waves *Phys. Plasmas* **11** 2349–76
- [43] Lin-Liu Y R, Chan V S and Prater R 2003 Electron cyclotron current drive efficiency in general tokamak geometry *Phys. Plasmas* **10** 4064–71
- [44] Gnesin S, Coda S, Decker J and Peysson Y 2008 Suprathermal electron studies in the TCV tokamak: design of a tomographic hard-x-ray spectrometer) *Rev. Sci. Instrum.* **79** 10F504
- [45] Peysson Y, Decker J and Morini L 2012 A versatile ray-tracing code for studying rf wave propagation in toroidal magnetized plasmas *Plasma Phys. Control. Fusion* **54** 045003
- [46] Poli E, Müller M, Zohm H and Kovari M 2019 Fast evaluation of the current drive efficiency by electron cyclotron waves for reactor studies *EPJ Web Conf.* **203** 01008
- [47] Fidone I and Giruzzi G 1990 Diagnosis of superthermal electrons using cyclotron radiation *Nucl. Fusion* **30** 803–13